SOFT ROBOTS

Translucent soft robots driven by frameless fluid electrode dielectric elastomer actuators

Caleb Christianson,[1] Nathaniel N. Goldberg,[2] Dimitri D. Deheyn,[3]
Shengqiang Cai,[4,5] Michael T. Tolley[4,5]*

Dielectric elastomer actuators (DEAs) are a promising enabling technology for a wide range of emerging applications, including robotics, artificial muscles, and microfluidics. This is due to their large actuation strains, rapid response rate, low cost and low noise, high energy density, and high efficiency when compared with alternative actuators. These properties make DEAs ideal for the actuation of soft submersible devices, although their use has been limited because of three main challenges: (i) developing suitable, compliant electrode materials; (ii) the need to effectively insulate the actuator electrodes from the surrounding fluid; and (iii) the rigid frames typically required to prestrain the dielectric layers. We explored the use of a frameless, submersible DEA design that uses an internal chamber filled with liquid as one of the electrodes and the surrounding environmental liquid as the second electrode, thus simplifying the implementation of soft, actuated submersible devices. We demonstrated the feasibility of this approach with a prototype swimming robot composed of transparent bimorph actuator segments and inspired by transparent eel larvae, leptocephali. This design achieved undulatory swimming with a maximum forward swimming speed of 1.9 millimeters per second and a Froude efficiency of 52%. We also demonstrated the capability for camouflage and display through the body of the robot, which has an average transmittance of 94% across the visible spectrum, similar to a leptocephalus. These results suggest a potential for DEAs with fluid electrodes to serve as artificial muscles for quiet, translucent, swimming soft robots for applications including surveillance and the unobtrusive study of marine life.

INTRODUCTION

Dielectric elastomer actuators (DEAs) show considerable potential in a variety of fields including microrobotics (*1*, *2*), bioinspired robotics (*3–5*), artificial muscles (*6*), and microfluidics (*7–9*). Their high energy efficiency and large active strains make them suitable for many applications that require low-power actuators with large strokes. Two recent efforts by Godaba *et al.* and Shintake *et al.* have developed underwater swimming actuation with DEAs in jellyfish- and fish-inspired robots (*10*, *11*). In their most basic form, DEAs are composed of an elastomeric dielectric sandwiched between a pair of compliant electrodes. The dielectric layer is typically a silicon- or acrylic-based polymer (e.g., polydimethylsiloxane or the Very High Bond (VHB) acrylic adhesive by 3M, respectively) (*12*, *13*). The electrodes are generally composed of deposited metals (*14*, *15*), carbon particles or nanotubes (*15*), ionogels (*16*, *17*), or ionic hydrogels (*18*, *19*).

However, challenges remain with using the aforementioned approaches to compliant electrodes for transparent swimming robots. Metallic electrodes provide excellent conductivity but add stiffness to the structure, which impedes the actuation (*15*). Although techniques exist to fabricate metallic films that are flexible and stretchable (*20–23*), these approaches require complex fabrication procedures and lead to at least partially opaque conductive layers. It is possible to make stretchable metallic electrodes using various methods; however, these methods still result in a stiff layer relative to the dielectric layer. As a result, most previous studies have used electrodes made of suspensions of carbon in a

soft or liquid carrier or of conductive hydrogels. Carbon particles suspended in silicone oil (e.g., carbon grease) is the material most commonly used for DEA electrodes, but it is challenging to pattern, prone to mechanical abrasion, and opaque. Moreover, carbon grease electrodes are subject to drying and diffusion of the silicone oil through the dielectric layer, which can swell the elastomer and affect the mechanical properties of the DEA over time (*15*). Whereas nonpolar liquids are known to induce swelling in dielectric elastomers, polar liquids are known to have a much higher compatibility with silicone elastomers and induce minimal swelling (*24*, *25*). Previous work has demonstrated the patterning of ionic hydrogels to serve as optically transparent electrodes (*18*, *19*, *26*). However, ionic hydrogel electrodes require encapsulation to prevent mechanical abrasion (*27*) and dehydration (*18*, *27*). Further, any conductive electrode with non-negligible stiffness reduces the efficiency of the DEA (*28*) and thus the performance of the actuator.

Ionic fluids represent an inexpensive, compliant, and transparent alternative for DEA electrodes (*25*). Fluidic electrodes have been used in DEAs to induce buckling of elastomer films on a microfluidic chip (*9*); in a thickened electrolyte solution for planar actuators (*29*); and for one of the two electrodes in a pressurized ballooning actuator (*30*), a bimorph actuator (*31*), and a fast-moving electronic robotic fish (*19*). Ionic fluid electrodes are especially interesting for use with DEAs in underwater environments or for fluid applications. The swimming DEAs presented by Godaba *et al.* (*10*) and Shintake *et al.* (*11*) rely on carbon-based electrodes, requiring the need for encapsulation layers and patterned electrode pairs found in both designs and imparting additional stiffness due to the electrode and encapsulation layers. A recent hybrid approach combining both hydrogel and fluid electrodes demonstrated a fast-moving soft electronic fish in which hydrogels served as one of the electrodes in a DEA, and the surrounding fluid was used as the ground electrode (*19*). However, this hybrid approach relies on hydrogel electrodes for the internal conductor, and the prestrained actuator necessitates a relatively rigid frame to maintain this prestrain. We
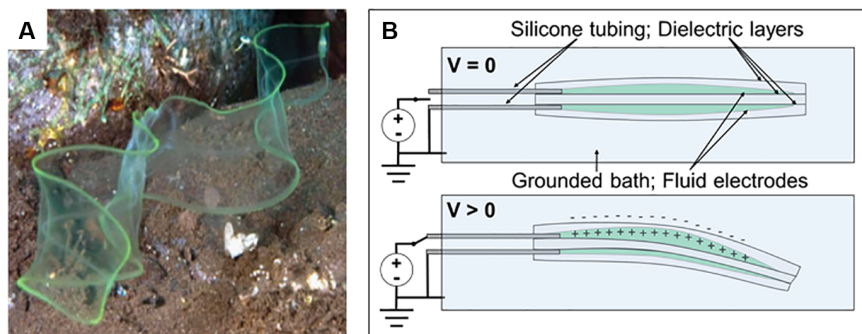
[1]Department of NanoEngineering, University of California, San Diego, 9500 Gilman Drive, La Jolla, CA 92093, USA. [2]Department of Mechanical Engineering, University of California, Berkeley, 6141 Etcheverry Hall, Berkeley, CA 94720, USA. [3]Marine Biology Research Division, Scripps Institution of Oceanography, 9500 Gilman Drive, La Jolla, CA 92093, USA. [4]Department of Mechanical and Aerospace Engineering, University of California, San Diego, 9500 Gilman Drive, La Jolla, CA 92093, USA. [5]Materials Science and Engineering Program, University of California, San Diego, 9500 Gilman Drive, La Jolla, CA 92093, USA.
*Corresponding author. Email: tolley@ucsd.edu

previously presented a simple frameless proof-of-concept bimorph actuator that showed some underwater motion and was straightforward and inexpensive to fabricate, consisting of water for electrodes and prestrain-free dielectric layers (*31*). However, this actuator was powered by a single pair of DEA modules and thus required a stiffer leading edge to generate asymmetric motion. Further, forward propulsion was only observed when the actuator pushed off the air-water interface during each stroke.

The transparency of both fluid and hydrogel electrodes suggests their potential for camouflaged applications, as recently demonstrated by the work of Li *et al.* (*19*) and Yuk *et al.* (*32*). The transparency of their devices enables passive camouflage, which eliminates the need for foreknowledge and adaptation to the background and surrounding environment, as required in active camouflage. In addition to camouflaged robotics, even partially transparent actuators open up a suite of promising applications, including flexible displays with haptic feedback or optic applications (*33*).

In this paper, we present a swimming robot inspired by leptocephali (Fig. 1A) and composed of frameless, transparent, bimorph DEA segments with fluid electrodes. We built upon our previous demonstration of a simple fluid electrode DEA (or FEDEA) bimorph (*31*) and demonstrated that a polar fluid, even one with low conductivity, can be used for both electrodes, obviating the need for hydrogel, carbon-based, or metallic electrodes. We present an approach to the design and fabrication of submerged actuators in which both electrodes were fluids and the surrounding fluid served as the second electrode, eliminating the need for patterning and fabricating both electrodes, which had been required in most previous DEAs. This simplified the design of the actuators and improved their efficiency by eliminating the need to add conductive and encapsulation layers that would stiffen the DEA. Because the fluid electrodes and dielectric elastomer are translucent, so is our swimming robot, enabling passive camouflage and optical communication. We achieved this with prestrain-free DEAs, eliminating the need for rigid frames to maintain the prestrain, resulting in a fully compliant actuator capable of continuous deformation. We demonstrated this approach with a proof-of-concept implementation of FEDEAs: translucent bimorph actuators for a submersible swimming soft robot.

RESULTS

Design of an FEDEA bimorph module

We designed and fabricated FEDEA bimorphs consisting of two separate fluid chambers enclosed by three layers of dielectric elastomer (Fig. 1B and fig. S1). When we submerged the actuator in a grounded fluid and applied a voltage to one of the fluid chambers in the actuator with respect to ground, the Maxwell pressure compressed the dielectric layer between the internal fluid and the external bath. This induced the chamber to elongate in the directions perpendicular to the electrical field, which caused the bimorph to bend away from the actuated side.

Analytical bending model

To develop an understanding of how the actuation of our bimorph module scales with its geometry, material properties, and the applied voltage, we used the elementary Euler-Bernoulli beam theory. We consider the actuator to be a collection of three layers of equal thickness h stacked on top of one another and examine the case in which one of the outer two layers is actuated, that is, the case where the bimorph undergoes a bending deformation, either upward or downward.

When a voltage is applied across one of the layers, opposing charge distributions build up on either side, causing an effective mechanical pressure p, which in turn results in a longitudinal strain in the said layer. An application of Hooke's law shows that this strain is given by

$$\varepsilon_{xx} = \frac{vp}{E} \tag{1}$$

where v and E are Poisson's ratio and the elastic modulus of the dielectric elastomer, respectively. Pelrine's equation (*12*) gives an expression for the equivalent mechanical pressure acting on the actuated layer:

$$p = \epsilon_0 \epsilon_r \left(\frac{V}{h}\right)^2 \tag{2}$$

Here, ϵ_0 is the permittivity of free space, ϵ_r is the relative permittivity of the dielectric elastomer, and V is the applied voltage. We now analyze the bimorph as a whole, approximating the collection of three layers as an Euler-Bernoulli beam of thickness $3h$ undergoing pure bending. It follows that the longitudinal strain is y/ρ, where y is the distance from the neutral axis and ρ is the curvature. Considering Eq. 1 to be the leading-order expression for the longitudinal strain in the extreme tensile fiber of the beam, we find, after dropping a constant of 3/2, that

$$\frac{h}{\rho} \sim \frac{vp}{E} \tag{3}$$

By inserting Eq. 2 into Eq. 3 and rearranging, we find the leading-order functional dependence of the curvature to be

$$\frac{1}{\rho} \sim \frac{v\epsilon_0\epsilon_r V^2}{Eh^3} \tag{4}$$

Fig. 1. Bioinspiration and working principle of FEDEA. (**A**) Photograph of leptocephalus (eel larva; length, about 400 mm) swimming underwater. Reprinted from Miller *et al.* (*59*), with permission from the authors. (**B**) Working principle of FEDEA bimorph module (not to scale): For bidirectional actuators, we make two DEAs from three layers of an acrylic elastomer adhesive. We created the active areas of the actuators by selectively passivating the surfaces of the adhesive with a powder, which allowed the conductive fluid to enter from the tubing and cover the active area. We connected the actuator to the high voltage lead of the power supply through the silicone tubing. Application of a voltage in one of the fluid chambers with respect to the external fluid induced Maxwell stress in the dielectric, inducing a bending motion away from the actuated side.

This result suggests that the curvature is proportional to the square of the applied voltage and inversely proportional to the thickness of the actuator to the third power. Furthermore, the curvature is expected to be independent of the actuator's length. Tests of actuators of three different lengths (73, 110, and 143 mm) generally agreed with the scaling relationship (4), as outlined in fig. S2. However, they showed a minor dependence of the curvature on the actuator's length, likely due to higher-order effects not captured in our simplified analysis, such as out-of-plane deformation and edge effects. In these experiments, we achieved a maximum curvature of 12.5 ± 0.4 m^{-1} with a 73-mm-long bimorph actuated at an initial electric field of 20 MV m^{-1} (10 kV applied to a 0.5-mm-thick film).

A small modification of the simple scaling relationship detailed in Eq. 4 has important consequences for the design of the actuators. If the radius of curvature is large compared with the length of the actuator, that is, $L/\rho \ll 1$, it can be shown that the transverse deflection δ of the actuator scales as

$$\delta \sim \frac{\nu \epsilon_0 \epsilon_r V^2 L^2}{E h^3} \qquad (5)$$

This basic scaling relationship describes the leading-order dependence of the actuator's motion on its geometry and applied voltage. It shows that the actuation depends on the length L and the thickness h, but considerably more strongly on the thickness. Hence, in designs where it is desirable to maximize the deflection, efforts should be focused on reducing h rather than increasing L, keeping in mind that a very small h would lead to dielectric breakdown and failure of the actuator. Designing around a small h rather than a large L has the added benefits of reducing the amount of material comprising the actuator, reducing costs, and suggesting the potential for miniaturization.

Influence of water conductivity

The bimorph actuators were tested using water with a salt concentration comparable to that of seawater (35 g liter^{-1}), deionized water, and United States Pharmacopeia (USP)–grade water (AquaPur, Decon) as both the internal and external fluids. We measured the conductivity of each of the three solutions and found them to be 48.15 ± 0.09, 0.045 ± 0.003, and 0.040 ± 0.002 mS cm^{-1}, respectively. To test the impact of water conductivity on actuator performance, we measured the maximum displacement of FEDEA bimorphs with matching internal and external fluids of either saltwater or USP-grade water and found that the maximum actuation amplitude at 1 Hz was 2.0 and 1.7 mm, respectively (fig. S3). This demonstrates that that there is only a moderate impact of performance on the conductivity of the solution, and for reasons of simplicity, we begin with deionized water as both the internal and external fluid for the actuators in the robot but make no efforts to maintain the purity of the water. The time constant of a highly resistive ionic solution is greater than that of a more conductive solution, as described by Keplinger et al. (18). However, it is still very small (on the order of 10^{-7} s), whereas the damping effects of the fluid viscosity and viscoelasticity of the elastomer (34, 35) have much slower time scales (order 10^0 to 10^3 s) and thus dominate the time scale of the response, leading to a negligible difference in the observed performance of actuators in solutions with different ionic concentrations. One implication of this result is that the fluid electrodes are compatible in both freshwater and seawater environments.

Bioinspiration for swimming and transparency

Eels move quickly and efficiently using an undulating motion as a traveling wave that traverses the body of the eel, known as anguilliform motion (36). To produce anguilliform motion, we designed our swimming robot as three bimorph FEDEA modules placed end to end in series (Fig. 2). The robot is 22 cm long, 5 cm tall, and 1.5 mm thick. To imitate the traveling wave actuation observed in swimming eels, we actuated these six actuators in sequence (see Fig. 2, right). We connected each actuator to a power supply through a silicone tube filled with water, which terminates at a metallic syringe tip, providing electrical contact between the fluid chamber and the control electronics (fig. S4). By controlling the sequence and timing of activation of the six actuators at a fixed voltage (7.5 kV), we generated an undulating motion in the robot (see Fig. 2 and movie S1). To generate a propulsive traveling wave, inspired by the undulating motions found in eels, we actuated diagonal pairs of chambers in sequence from the anterior to posterior sections of the robot, as shown in Fig. 2.

Further, eel larvae, also known as leptocephali, are translucent. Inspired by this, we designed our proof-of-concept swimming robot to be translucent. Because the internal electrode was a conductive fluid and the dielectric elastomer is a transparent membrane, the robot is transparent, with the exception of some residual hazing caused by the passivating agent used to pattern the electrodes (see Materials and Methods).

Swimming performance of the FEDEA

Because the FEDEA actuators consist of materials with densities that are comparable to water, they face reduced buoyancy challenges found in pneumatically actuated fish-like soft robots (37). To maintain a consistent swimming depth for performance characterization, we tuned the actuator to be negatively buoyant and suspended the actuator from a floating boom (Fig. 2). The wetted areas of the actuator, tubing, and boom are 230, 23, and 270 cm^2, respectively. By sequential activation of the electrodes, we generated an undulating motion, enabling forward propulsion. We measured a maximum swimming speed of 1.9 mm s^{-1} (0.009 body lengths per second) at a driving frequency of 0.33 Hz. To better understand the performance of this proof-of-concept robot, we
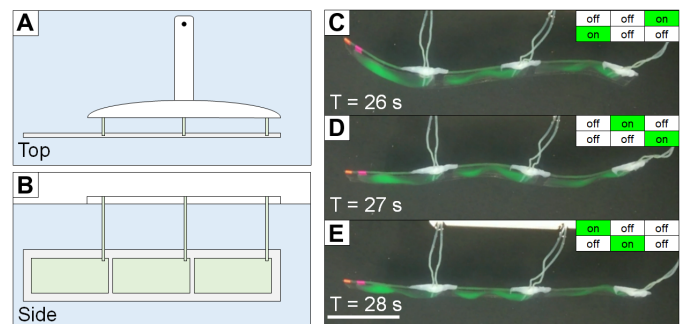
Fig. 2. Schematic of experimental setup and screen captures from swimming. Top-down (**A**) and side (**B**) view schematics of the experimental setup. The robot comprised three FEDEA bimorph modules arranged end to end. The motion of the swimmer was planarized by suspending it from a rotating boom by the tubing connected to each actuator. The boom permitted the robot to swim at a fixed depth in a large arc, reducing the impact of lateral tube tension on the robot's performance. (**C** to **E**) Top-down view of the actuator with time indicated. Inset diagram is a top-down schematic describing which of the six DEAs are at rest ("off") or actuated ("on") in that frame. We cycled through the three states shown at a rate of 0.33 Hz, resulting in an average forward speed of 1.9 mm s^{-1}. Scale bar, 5 cm.

calculated the mean thrust and Froude propulsive efficiency η_{EBT} based on Lighthill's elongated body theory (EBT) (36, 38–40). We found the parameters needed for calculating the thrust and Froude efficiency based on EBT (i.e., amplitude, wavelength, and wave speed) by fitting to the experimental data of the position of the tail of the robot over time. (For further discussion of the fitting and calculations, please see text S1.) We estimated the efficiency of the robot using Lighthill's EBT as $\eta_{EBT} = 1 - \frac{V-U}{2V}$, where U is the mean swimming speed and V is the wave speed. For a driving frequency of 0.33 Hz, we measured a wave speed of 0.055 m s^{-1}, resulting in a η_{EBT} of 52%. The measured Froude efficiency informs us that excess effort is wasted in generating lateral motion in our robot; only about half of the effort is converted into useful thrust. One metric of swimming efficiency is the Strouhal number (41), which is proportional to the product of the tail-beat amplitude and driving frequency and inversely proportional to the velocity. As a preliminary optimization of the swimming gait of the robot, we measured the amplitude as a function of driving frequency for an FEDEA bimorph (fig. S6). From this, we observed a peak value of the product at a driving frequency of 0.5 Hz. When we increased the actuation frequency of the multisegmented robot from 0.33 to 0.5 Hz, we observed a 12% increase in average swimming speed for the same actuation sequence. This demonstrates the opportunity for further optimization of the actuation sequence and frequency. For consistency, the results described in the remainder of the paper refer to the performance of the robot actuated at 0.33 Hz.

Power consumption during actuation

We calculated the electrical power input that the robot consumed to be 34 mW based on the change in capacitance as $P_{electrical} = C_{act}V^2f$, where C_{act} is the capacitance of the actuator when charged, V is the applied potential, and f is the driving frequency. The capacitance at rest was measured directly with an inductance, capacitance, and resistance (LCR) meter, and the capacitance when actuated was calculated based on the deformation of the area and thickness of the robot based on Hooke's law and Pelrine's equation (12). We also calculated the power consumption experimentally by measuring the voltage and current in a single actuator during a charge and discharge cycle and found the total power consumption for the robot (six actuators) to be ~20 mW, which is comparable with the calculated value based on the change in capacitance. We calculated the mean thrust using EBT to be 0.25 mN over three tail-beat cycles at a driving frequency of 0.33 Hz (see text S1 for details). We also measured the thrust experimentally and found a mean thrust of 42 ± 7 μN (see text S2). Taking the lower of these two values, the mean power output based on the experimentally measured thrust was 0.08 μW, and power density was 3.2 μW kg^{-1} for an actuator mass of 25.1 g. The power efficiency of the actuator, based on the mean thrust and electrical power input ($\eta = P_{thrust}/P_{electrical}$), was 0.0013%. Whereas the η_{EBT} describes the relationship between lateral motion and useful forward propulsion, the power efficiency here shows that about 0.0013% of electrical power used to deform the actuator results in thrust.

Acoustic profile demonstrating the sonic stealth potential of the robot

One advantage of using DEAs for underwater propulsion is the ability of our soft robot to move quietly, which is of considerable importance in stealth and acoustic monitoring applications. To demonstrate the quiet propulsion of our robot, we recorded the acoustic profile of FEDEA actuators in water at rest and during actuation and showed that there was only a slight increase in measured sound with an average value of 0.3 dB when the actuators were running (fig. S6).

Translucency for optical camouflage

For applications where transparency or passive camouflage is desired, the robot should exhibit high transmittance throughout the visible spectrum (Fig. 3). To quantify the translucency, we measured light transmission through the actuator. There were two visibly distinct regions in the actuator: the border, which consisted of three layers of a transparent acrylic elastomer, and the active area, where the fluid electrodes resided. Using hyperspectral imaging (42, 43), we found that the active area had a transmittance of 97% compared with the border transmittance of 90%. The higher transmittance of the active area may be due to an improvement of light transmission through the water-elastomer interfaces in the area, which are diminished in the air-elastomer interfaces around the border. As a comparison, we measured the transmittance in the abdomen of a leptocephalus that uses translucency for camouflage (32). We found that the transmittance of the two areas of the actuator was comparable to that of the eel, which had an average transmittance of 94% (Fig. 3D).

Visual communication using fluorescence

In addition to passive camouflage, the high transmittance of the robot enables visual display through the body of the robot for communication. Recently, species of brightly fluorescent eels have been found in the Caribbean Sea (44). Although the purpose of the biofluorescence is still up for debate (45), one purpose may be to help eels locate each other during full moon spawning events. Other proposed functions may be to aid in communication, predator avoidance, or prey attraction. In robotic applications, fluorescence may be a way to enable communication optically in an environment that is not conducive to radio communication (46). To test the feasibility of encapsulating a fluorescing dye within our actuators, we injected green fluorescent protein (GFP) between two layers of the dielectric film (in a similar configuration to the fluid electrodes described above) and plotted the initial and subsequent emission spectrum after 2 days of storage in the dark at room temperature (Fig. 4A). These results showed that the fluorescence response of the GFP within the actuators did not decay substantially after 48 hours of encapsulation.

For larger volume testing, we then introduced a low-cost, non-GFP commercial dye that fluoresces under ultraviolet (UV) excitation into the actuation chambers of our swimming robot. We then excited the dye with UV illumination while simultaneously actuating the robot (see Fig. 4, B and C, and movie S1). Taking advantage of the high transmittance of the actuator, we were able to use the entire internal electrode area for display, simultaneously maximizing the size of the DEA and the display.

DISCUSSION

The proof-of-concept design here demonstrates that water, including the surrounding fluid in submerged devices, can be used as compliant electrodes for DEAs. This design approach obviates the need for the use of hydrogel-, carbon-, or metal-based electrodes and potentially simplifies the design of actuators for submersible robots that can take advantage of the ground potential provided by the surrounding fluid. The results in fig. S3 show that FEDEAs can provide greater actuation amplitudes than non-prestrained actuators with carbon grease. When a bimorph with carbon grease electrodes is submerged in water, the maximum amplitude decreases by 46%. However, the amplitude is about two times larger for FEDEAs with USP-grade water compared with submerged carbon grease electrodes. This demonstrates that the actuation performance decreases when the actuators are submerged in water, but fluid electrodes provide comparable, if not improved, actuation performance over carbon grease electrodes when submerged.
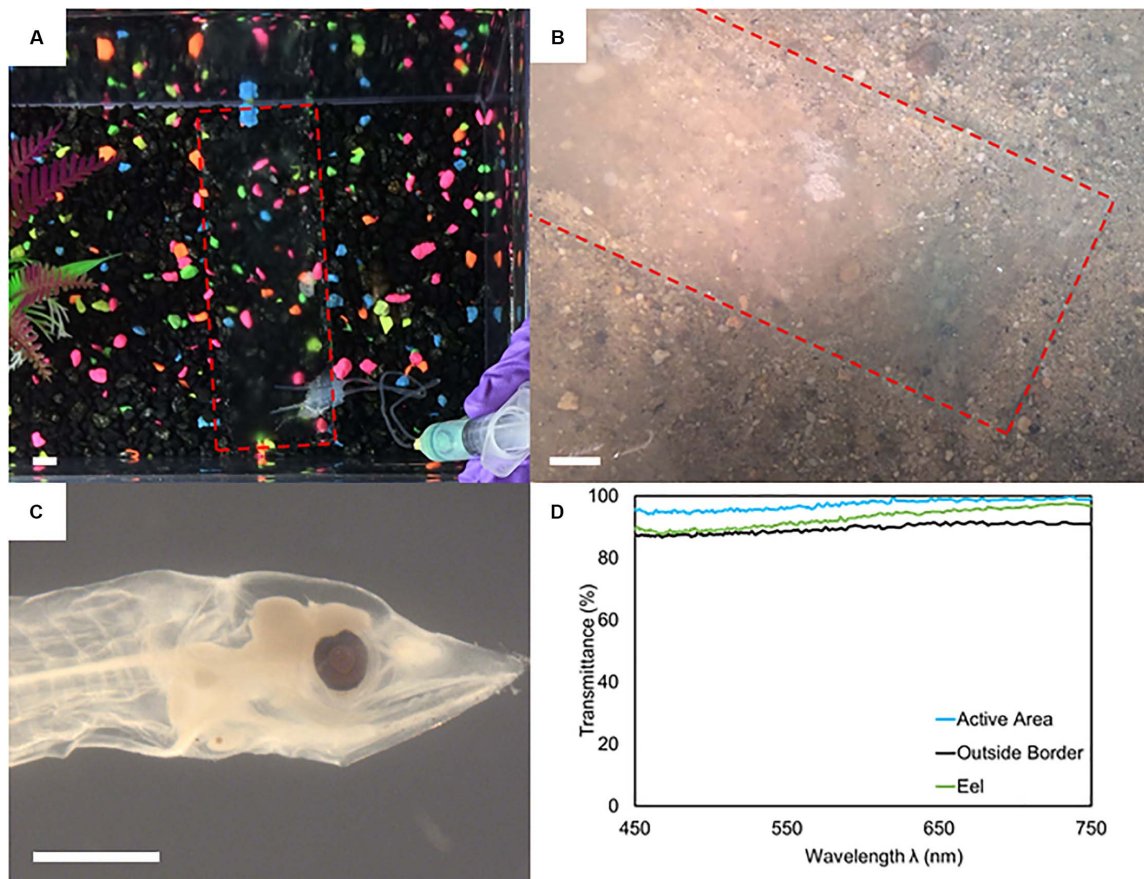
Fig. 3. Demonstration of translucency. Photographs of the actuator over backgrounds of aquarium rocks (**A**) and sand (**B**), with dotted lines indicating the edge of the actuator. (**C**) Microphotograph of leptocephalus (only head shown) from the Scripps Institution of Oceanography (SIO) Marine Vertebrate Collection, illustrating the high transparency of the eel. (**D**) Transmission spectrum taken by hyperspectral imaging for two distinct regions in the actuator (active area, where the fluid electrodes are located, and the outside border) compared with the eel, demonstrating that the two sections of the actuator are in the range of transmittance values of the eel in the visible spectrum. Scale bars, 1 cm [(A) and (B)] and 1 mm (C).

One advantage of compliant actuators and soft robotics in general is the ability to minimize the risk of damage to their surroundings, especially when interacting with living creatures, unstructured environments, or delicate objects (*47–50*). The prototype robot presented here consists of completely soft, submersible actuators that take advantage of the conductivity and potential of its surrounding environment. Further, because the actuator is completely soft, it reduces the risk of harming wildlife or fragile structures in the case of contact between the robot and its environment.

One challenge with the current design is that the structure has a preferential direction of bending, resulting in asymmetric actuation about the midline of the robot. We believe that this is due to a slight curvature in the robot caused by our manufacturing approach, which imparts a preferential bending direction in the actuators, resulting in larger bending in one direction, as shown in Fig. 2. Furthermore, the bidirectional expansion of the actuated bimorph sections causes curvature in two directions that seems to inhibit bidirectional bending of the segments. A conceptual constraint of fluid electrodes is that they are not amenable to all actuator configurations, in that one of the electrodes generally requires some encapsulation to define its geometry and ensure its contact with the DE membrane. The design and fabrication approaches described in this work also have a few additional design constraints: (i) the

border around the electrodes needs to be at least ~8 mm wide to ensure adhesion and reduce the risk of shorting; (ii) tubing is required to inject the fluid and maintain electrical contact, which must be free of air bubbles; and (iii) a sealant is required to prevent leakage around the tubing/elastomer interface. One potential way to address these challenges, and potentially scale to smaller dimensions, is to use soft lithography, as used previously for DEA pumps (*51, 52*).

The actuator itself is neutrally buoyant, which reduces the need to overcome the negative buoyancy found in most, traditional underwater robotic systems. It is possible to fine-tune the buoyancy by introducing air into the fluid chambers or by ballasting to achieve negative buoyancy. The speed of our robot is slower than most reported underwater swimmers using smart actuators (*53, 54*), but previous swimmers based on DEAs either are opaque (because of electrode materials) or require prestrained dielectric membranes, or both. The boom serves to planarize the motion of the robot so that we can better characterize its performance. However, the boom also increases the drag resisting the motion of the robot. Because the robot is operating in laminar flow (Reynolds number of ~450), it experiences viscous drag proportional to the combined wetted area of the robot, tubing, and boom. The actuator comprises 44% of the wetted area of the setup, indicating that the performance described here is a conservative estimate of the potential
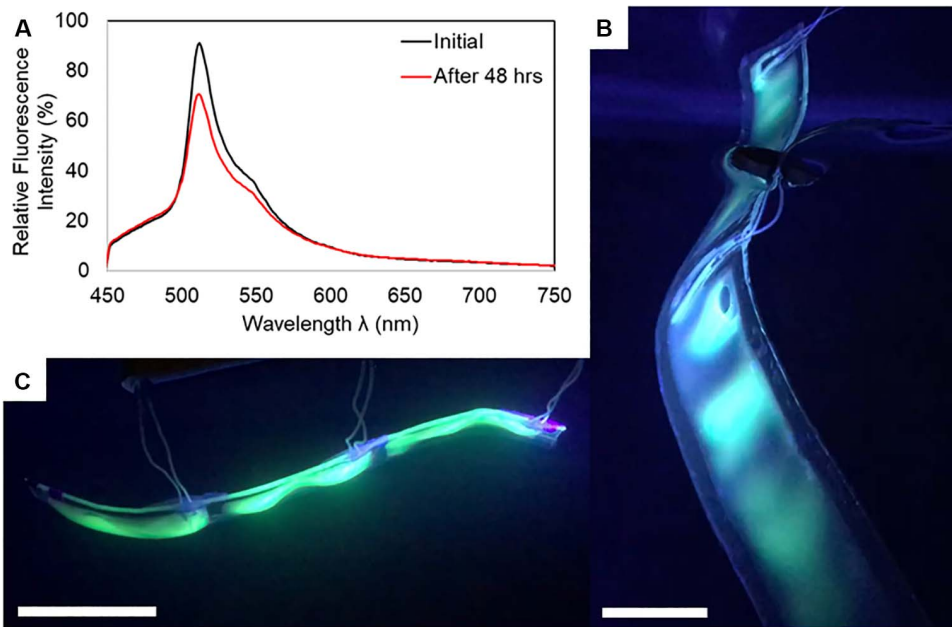
Fig. 4. Fluorescence response of actuator. (**A**) Emission spectrum (excitation at 390 nm) of commercially purchased GFP embedded between two layers of VHB measured initially after injection of GFP and after 48 hours of storage in the dark at room temperature. (**B** and **C**) Photos of actuator fluorescing under UV/blue light stimulation. Scale bars, 5 cm.

performance of the robot. Without this increased drag, we estimated the steady-state velocity of the robot to be $v' = 1/0.44 \times 1.9$ mm s^{-1} = 4.3 mm s^{-1}. The efficiency of our robot is less than the estimated η_{EBT} of swimming eels, which has been reported to range from 87 to 97% (40); however, the proof-of-concept actuation sequence presented here has not been optimized for speed or efficiency. One way to estimate the potential optimized performance of the robot is through EBT. If we were able to improve our robot such that it matched the efficiency of natural eels at a fixed body wave speed (e.g., by optimizing the parameters of the EBT model, nominally the amplitude at the tail, A; the amplitude growth rate, α; the length of the eel, L; and the wavelength of the actuation, λ) (55), then EBT predicts that we could expect a maximum speed of 55 mm/s.

As another point of comparison, the power efficiency of a commercially available remotely operated vehicle (ROV), the Trident by OpenROV, is estimated to be 15% (56, 57). The Trident ROV has a maximum speed of 2 m s^{-1} and a run time of 3 to 4 hours on a 389-kJ battery that weighs 0.57 kg, resulting in a range of 22 to 29 km (56). Although the FEDEAs of our robot required very little power to generate thrust, the driving electronics consumed a comparatively large amount of energy. Our prototype circuit, which was not optimized for efficiency, consumed about 1 W during actuation, primarily due to discharging the DEAs through resistors. Because the robot reached an average speed of 1.9 mm s^{-1}, it is possible to estimate that if we powered it with a 389-kJ battery (without affecting the hydrodynamic drag), our robot would have an estimated range of ~0.7 km.

Although the speeds and efficiencies of the DEAs reported in (10, 11, 19) are much higher than those described in this work, we have done so without any prestrain, eliminating the need for rigid or semi-rigid members to maintain a stretch. This results in a fully soft elastomeric robot. For example, the speed and efficiency of the work by Li *et al.* are 71 and 7900 times greater than that of our robot, respectively (19). However, their work does not perform as well on camouflage and conform-

ability. Although our submerged robots have a longevity of 10^2 to 10^3 cycles, we have observed that the elastomer membranes themselves can withstand over 10^6 actuation cycles and ~300 hours of continuous immersion in fluid (see text S3). Further improvements to the efficiency, range, and longevity of the robot are left for future work.

Because the robot is driven by DEAs, its propulsion system is silent, especially compared with propeller or jet thrusters used on typical ROVs. Optical transparency enables passive camouflage so that the robot can blend into its environment, and the combination of optical and acoustic stealth suggests the potential for underwater applications where detection or disturbance of the environment is undesirable. Recent work has explored electroluminescence in translucent soft robotics (58), which could be implemented in our swimming robot, enabling a more controllable, programmable display. We can implement optical communication through fluorescence, electroluminescence, or other techniques to enable alternative means of localization or communication underwater (58). A fully contained soft robot driven by these fluid electrode DEAs could house miniature high-voltage dc (HVDC) convertors, a microcontroller, cameras, sensors, and a battery, which could be encapsulated in a watertight chamber that is electrically isolated from the surrounding fluid, as previously demonstrated for prestrained DEA swimmers (19). This would enable quiet, untethered, submersible, passively camouflaged soft robotics for search and rescue or ocean discovery operations.

MATERIALS AND METHODS
Actuator fabrication
To construct the bimorph actuator module, we attached two layers of an acrylic adhesive (VHB 4905, 3M) to each other (fig. S1). We patterned the electrode chambers with a passivating agent (corn starch for bimorph characterization and superfine granulated sugar and dishwashing liquid for transparency and swimming experiments) to prevent adhesion between the layers in these regions. We inserted a silicone tube to enable the injection of a conductive fluid into the electrode chamber via a syringe. We used water as the conductive ionic solution, and we added food dye to the internal conductive solution as a visual aid for the bimorph and some swimming experiments. The water that fills the actuators and the tank for swimming experiments was initially deionized, but we made no efforts to protect the purity of the water in the tank.

Characterization of actuation and swimming
We connected the fluid to a high-voltage power supply through the metallic needle of the syringe, which provided electrical contact to the fluid within the actuator. A high-voltage power supply (ES20P-5W, Gamma High Voltage Research Inc.) provided the power for the bimorph actuator module curvature measurements. EMCO high-voltage dc converters amplified the signal from a microcontroller (Arduino Uno) for the swimming experiments. We used a camera phone to record images and

video in all experiments. We used the open source Tracker Video Analysis Tool (www.physlets.org/tracker) for motion tracking of the robot.

Fluorescence response

We used "Green UV Laser Dye" (Bitspower) as the dye and a light-emitting diode flashlight (TaoTronics; excitation spectrum, 395 to 400 nm) as a UV source in the fluorescing swimming experiments. We used a hyperspectral imaging system (PARISS hyperspectral imager, LightForm Inc.) mounted on a Nikon Eclipse 80i microscope to measure the fluorescence spectrum from commercially sourced GFP embedded between layers of the dielectric elastomer in the longevity study. We plotted the spectra from 450 to 750 nm for evaluation of the longevity of the emission of the embedded GFP both initially after embedding the GFP and 48 hours later.

Translucency study

We measured the transmission of regions of interest in the robot and the leptocephalus with the PARISS hyperspectral imaging system. We selected two regions in the robot (around the outside border of the robot and over the active area) and one region in the leptocephalus to compare their transmission between 400 and 800 nm.

Acoustic measurements

To measure the acoustic profile of the robot, we used a hydrophone (Teledyne Reson) about 5 cm away from bimorph FEDEAs within a ~700-ml water tank. We measured the sound both when the actuators were sitting at rest for a background signal and when we actuated the bimorphs at 0.33 Hz. We recorded the signal with a Sound Devices 722 high-resolution digital audio recorder and analyzed the spectrum with Audacity using a Hanning window and a size of 1024.

Conductivity measurements

Data were obtained using a potentiostat (PalmSens 4, Enschede, Holland), on a three-electrode system consisting of a 4-mm-diameter gold working electrode, a gold counter electrode, and a Ag/AgCl reference electrode (DRP-220AT, Dropsens, Oviedo, Spain). Impedance measurements were taken with electrochemical impedance spectroscopy starting at 0 V versus a Ag/AgCl reference electrode using ac signals with a peak to peak amplitude of 10 mV in frequencies from 5 to 100,000 Hz. Conductivity of the solution was calculated using the equation $\kappa = \frac{A}{Zl}$, where κ is the conductivity of the solution, A is the area of the electrode, Z is the impedance at 100 kHz, and l is the length between electrodes.

SUPPLEMENTARY MATERIALS

robotics.sciencemag.org/cgi/content/full/3/17/eaat1893/DC1
Text S1. Swimming performance calculations.
Text S2. Experimental measurement of thrust.
Text S3. Longevity study.
Fig. S1. Fabrication process for bidirectional fluid electrode DEA.
Fig. S2. Bimorph experimental setup, images, and results.
Fig. S3. Performance comparison of carbon grease and FEDEA bimorphs.
Fig. S4. Photograph and schematic of experimental setup.
Fig. S5. Comparison of experimental data and kinematic model.
Fig. S6. Effect of actuation frequency for a bimorph FEDEA underwater.
Fig. S7. Sound intensity results.
Table S1. Fitting parameters for sinusoid kinematic model of the tail.
Movie S1. Video of robot swimming under regular and UV light.

REFERENCES AND NOTES

1. R. E. Pelrine, R. D. Kornbluh, J. P. Joseph, Electrostriction of polymer dielectrics with compliant electrodes as a means of actuation. *Sens. Actuators A Phys.* **64**, 77–85 (1998).
2. R. D. Kornbluh, R. Pelrine, J. Joseph, R. Heydt, Q. Pei, S. Chiba, High-field electrostriction of elastomeric polymer dielectrics for actuation. *Proc. SPIE* **3669**, 149–161 (1999).
3. F. Carpi, S. Bauer, D. De Rossi, Stretching dielectric elastomer performance. *Science* **330**, 1759–1761 (2010).
4. I. A. Anderson, T. A. Gisby, T. G. McKay, B. M. O'Brien, E. P. Calius, Multi-functional dielectric elastomer artificial muscles for soft and smart machines. *J. Appl. Phys.* **112**, 041101 (2012).
5. D. Rus, M. T. Tolley, Design, fabrication and control of soft robots. *Nature* **521**, 467–475 (2015).
6. P. Brochu, Q. Pei, Advances in dielectric elastomers for actuators and artificial muscles. *Macromol. Rapid Commun.* **31**, 10–36 (2010).
7. C. Murray, D. McCoul, E. Sollier, T. Ruggiero, X. Niu, Q. Pei, D. Di Carlo, Electro-adaptive microfluidics for active tuning of channel geometry using polymer actuators. *Microfluid. Nanofluidics* **14**, 345–358 (2013).
8. B. Tavakol, M. Bozlar, C. Punckt, G. Froehlicher, H. A. Stone, I. A. Aksay, D. P. Holmes, Buckling of dielectric elastomeric plates for soft, electrically active microfluidic pumps. *Soft Matter* **10**, 4789–4794 (2014).
9. B. Tavakol, D. P. Holmes, Voltage-induced buckling of dielectric films using fluid electrodes. *Appl. Phys. Lett.* **108**, 112901 (2016).
10. H. Godaba, J. Li, Y. Wang, J. Zhu, A soft jellyfish robot driven by a dielectric elastomer actuator. *IEEE Robot. Autom. Lett.* **1**, 624–631 (2016).
11. J. Shintake, H. Shea, D. Floreano, Biomimetic underwater robots based on dielectric elastomer actuators. *2016 IEEE/RSJ Int. Conf. Intell. Robot. Syst.* **2**, 4957–4962 (2016).
12. R. Pelrine, R. Kornbluh, Q. Pei, J. Joseph, High-speed electrically actuated elastomers with strain greater than 100%. *Science* **287**, 836–839 (2000).
13. F. Carpi, I. Anderson, S. Bauer, G. Frediani, G. Gallone, M. Gei, C. Graaf, C. Jean-Mistral, W. Kaal, G. Kofod, M. Kollosche, R. Kornbluh, B. Lassen, M. Matysek, S. Michel, S. Nowak, B. O'Brien, Q. Pei, R. Pelrine, B. Rechenbach, S. Rosset, H. Shea, Standards for dielectric elastomer transducers. *Smart Mater. Struct.* **24**, 105025 (2015).
14. S. H. Low, L. L. Shiau, G.-K. Lau, Large actuation and high dielectric strength in metallized dielectric elastomer actuators. *Appl. Phys. Lett.* **100**, 182901 (2012).
15. S. Rosset, H. R. Shea, Flexible and stretchable electrodes for dielectric elastomer actuators. *Appl. Phys. A Mater. Sci. Process.* **110**, 281–307 (2013).
16. B. Chen, J. J. Lu, C. H. Yang, J. H. Yang, J. Zhou, Y. M. Chen, Z. Suo, Highly stretchable and transparent ionogels as nonvolatile conductors for dielectric elastomer transducers. *ACS Appl. Mater. Interfaces* **6**, 7840–7845 (2014).
17. X. Ji, S. Rosset, H. R. Shea, Soft tunable diffractive optics with multifunctional transparent electrodes enabling integrated actuation. *Appl. Phys. Lett.* **109**, 191901 (2016).
18. C. Keplinger, J.-Y. Sun, C. C. Foo, P. Rothemund, G. M. Whitesides, Z. Suo, Stretchable, transparent, ionic conductors. *Science* **341**, 984–987 (2013).
19. T. Li, G. Li, Y. Liang, T. Cheng, J. Dai, X. Yang, B. Liu, Z. Zeng, Z. Huang, Y. Luo, T. Xie, W. Yang, Fast-moving soft electronic fish. *Sci. Adv.* **3**, e1602045 (2017).
20. N. Bowden, S. Brittain, A. G. Evans, J. W. Hutchinson, G. M. Whitesides, Spontaneous formation of ordered structures in thin films of metals supported on an elastomeric polymer. *Nature* **393**, 146–149 (1998).
21. D.-H. Kim, J. A. Rogers, Stretchable electronics: Materials strategies and devices. *Adv. Mater.* **20**, 4887–4892 (2008).
22. D.-H. Kim, J. Xiao, J. Song, Y. Huang, J. A. Rogers, Stretchable, curvilinear electronics based on inorganic materials. *Adv. Mater.* **22**, 2108–2124 (2010).
23. R. Verplancke, F. Bossuyt, D. Cuypers, J. Vanfleteren, Thin-film stretchable electronics technology based on meandering interconnections: Fabrication and mechanical performance. *J. Micromechanics Microengineering.* **22**, 015002 (2012).
24. J. N. Lee, C. Park, G. M. Whitesides, Solvent compatibility of poly(dimethylsiloxane)-based microfluidic devices. *Anal. Chem.* **75**, 6544–6554 (2003).
25. A. Poulin, L. Maffli, S. Rosset, H. Shea, Interfacing dielectric elastomer actuators with liquids. *Proc. SPIE* **9430**, 943011 (2015).
26. J. A. Rogers, A clear advance in soft actuators. *Science* **341**, 968–969 (2013).
27. P. Calvert, Hydrogels for soft machines. *Adv. Mater.* **21**, 743–756 (2009).
28. M. Bozlar, C. Punckt, S. Korkut, J. Zhu, C. C. Foo, Z. Suo, I. A. Aksay, Dielectric elastomer actuators with elastomeric electrodes. *Appl. Phys. Lett.* **101**, 091907 (2012).
29. F. Carpi, P. Chiarelli, A. Mazzoldi, D. De Rossi, Electromechanical characterisation of dielectric elastomer planar actuators: Comparative evaluation of different electrode materials and different counterloads. *Sens. Actuators A Phys.* **107**, 85–95 (2003).
30. H. Godaba, C. C. Foo, Z. Q. Zhang, B. C. Khoo, J. Zhu, Giant voltage-induced deformation of a dielectric elastomer under a constant pressure. *Appl. Phys. Lett.* **105**, 112901 (2014).
31. C. Christianson, N. Goldberg, S. Cai, M. T. Tolley, in *Electroactive Polymer Actuators and Devices (EAPAD) XIX* (SPIE, 2017), p. 101631O.
32. H. Yuk, S. Lin, C. Ma, M. Takaffoli, N. X. Fang, X. Zhao, Hydraulic hydrogel actuators and robots optically and sonically camouflaged in water. *Nat. Commun.* **8**, 14230 (2017).
33. K. Wang, G. Ouyang, X. Chen, H. Jakobsen, Engineering electroactive dielectric elastomers for miniature electromechanical transducers. *Polym. Rev.* **57**, 369–396 (2017).

34. P. Sommer-Larsen, G. Kofod, M. H. Shridhar, M. Benslimane, P. Gravesen, Performance of dielectric elastomer actuators and materials. *Soc. Photo Optical Instrum. Eng. Conf. Ser.* **4695**, 158–166 (2002).

35. S. Michel, X. Q. Zhang, M. Wissler, C. Löwe, G. Kovacs, A comparison between silicone and acrylic elastomers as dielectric materials in electroactive polymer actuators. *Polym. Int.* **59**, 391–399 (2010).

36. M. J. Lighthill, Aquatic animal propulsion of high hydromechanical efficiency. *J. Fluid Mech.* **44**, 265–301 (1970).

37. A. D. Marchese, C. D. Onal, D. Rus, Autonomous soft robotic fish capable of escape maneuvers using fluidic elastomer actuators. *Soft Robot.* **1**, 75–87 (2014).

38. M. J. Lighthill, Note on the swimming of slender fish. *J. Fluid Mech.* **9**, 305–317 (1960).

39. M. J. Lighthill, Large-amplitude elongated-body theory of fish locomotion. *Proc. R. Soc. Lond. B* **179**, 125–138 (1971).

40. E. D. Tytell, The hydrodynamics of eel swimming I. Wake structure. *J. Exp. Biol.* **207**, 1825–1841 (2004).

41. G. S. Triantafyllou, M. S. Triantafyllou, M. A. Grosenbaugh, Optimal thrust development in oscillating foils with application to fish propulsion. *J. Fluids Struct.* **7**, 205–224 (1993).

42. J. R. A. Taylor, J. M. Gilleard, M. C. Allen, D. D. Deheyn, Effects of CO_2-induced pH reduction on the exoskeleton structure and biophotonic properties of the shrimp *Lysmata californica*. *Sci. Rep.* **5**, 10608 (2015).

43. A. Holzinger, M. C. Allen, D. D. Deheyn, Hyperspectral imaging of snow algae and green algae from aeroterrestrial habitats. *J. Photochem. Photobiol. B Biol.* **162**, 412–420 (2016).

44. D. F. Gruber, J. P. Gaffney, S. Mehr, R. DeSalle, J. S. Sparks, J. Platisa, V. A. Pieribone, Adaptive evolution of eel fluorescent proteins from fatty acid binding proteins produces bright fluorescence in the marine environment. *PLOS ONE* **10**, e0140972 (2015).

45. C. Mazel, Method for determining the contribution of fluorescence to an optical signature, with implications for postulating a visual function. *Front. Mar. Sci.* **4**, 266 (2017).

46. N. Farr, A. Bowen, J. Ware, C. Pontbriand, M. Tivey, An integrated, underwater optical/acoustic communications system, in *OCEANS 2010 IEEE* (IEEE, 2010), pp. 1–6.

47. L. U. Odhner, L. P. Jentoft, M. R. Claffee, N. Corson, Y. Tenzer, R. R. Ma, M. Buehler, R. Kohout, R. D. Howe, A. M. Dollar, A compliant, underactuated hand for robust manipulation. *Int. J. Rob. Res.* **33**, 736–752 (2014).

48. N. W. Bartlett, M. T. Tolley, J. T. B. Overvelde, J. C. Weaver, B. Mosadegh, K. Bertoldi, G. M. Whitesides, R. J. Wood, A 3D-printed, functionally graded soft robot powered by combustion. *Science* **349**, 161–165 (2015).

49. P. Polygerinos, N. Correll, S. A. Morin, B. Mosadegh, C. D. Onal, K. Petersen, M. Cianchetti, M. T. Tolley, R. F. Shepherd, Soft Robotics: Review of fluid-driven intrinsically soft devices; manufacturing, sensing, control, and applications in human-robot interaction. *Adv. Eng. Mater.* **19**, 1700016 (2017).

50. K. Kumar, J. Liu, C. Christianson, M. Ali, M. T. Tolley, J. Aizenberg, D. E. Ingber, J. C. Weaver, K. Bertoldi, A biologically inspired, functionally graded end effector for soft robotics applications. *Soft Robot.* **4**, 317–323 (2017).

51. J. J. Loverich, I. Kanno, H. Kotera, Concepts for a new class of all-polymer micropumps. *Lab Chip* **6**, 1147 (2006).

52. C. Christianson, N. N. Goldberg, M. T. Tolley, Elastomeric diaphragm pump driven by fluid electrode dielectric elastomer actuators (FEDEAs), in *Electroactive Polymer Actuators and Devices (EAPAD) XX* (SPIE, 2018), p. 105940O.

53. W.-S. Chu, K.-T. Lee, S.-H. Song, M.-W. Han, J.-Y. Lee, H.-S. Kim, M.-S. Kim, Y.-J. Park, K.-J. Cho, S.-H. Ahn, Review of biomimetic underwater robots using smart actuators. *Int. J. Precis. Eng. Man.* **13**, 1281–1292 (2012).

54. Q. Shen, T. Wang, J. Liang, L. Wen, Hydrodynamic performance of a biomimetic robotic swimmer actuated by ionic polymer-metal composite. *Smart Mater. Struct.* **22**, 075035 (2013).

55. E. D. Tytell, The hydrodynamics of eel swimming II. Effect of swimming speed. *J. Exp. Biol.* **207** (Pt. 19), 3265–3279 (2004).

56. Trident Underwater Drone | OpenROV Underwater Drones; www.openrov.com/.

57. Turnigy Aerodrive DST-700 Brushless Outrunner motor 700kv; https://hobbyking.com/en_us/turnigy-aerodrive-dst-700-brushless-outrunner-motor-700kv.html.

58. C. Larson, B. Peele, S. Li, S. Robinson, M. Totaro, L. Beccai, B. Mazzolai, R. Shepherd, Highly stretchable electroluminescent skin for optical signaling and tactile sensing. *Science* **351**, 1071–1074 (2016).

59. M. J. Miller, R. Rutgers, B. Haythorne, T. Yavuzdoğan, S. Obata, T. Wu, H. Rutgers, J. Powell, K. Tsukamoto, Observations of large muraenid leptocephali in coastal Indonesia: Locations of sightings and behaviour of the larvae. *Mar. Biodivers. Rec.* **6**, e82 (2013).

Science Robotics

Translucent soft robots driven by frameless fluid electrode dielectric elastomer actuators

Caleb Christianson, Nathaniel N. Goldberg, Dimitri D. Deheyn, Shengqiang Cai and Michael T. Tolley

ARTICLE TOOLS	http://robotics.sciencemag.org/content/3/17/eaat1893
SUPPLEMENTARY MATERIALS	http://robotics.sciencemag.org/content/suppl/2018/04/23/3.17.eaat1893.DC1
REFERENCES	This article cites 54 articles, 10 of which you can access for free http://robotics.sciencemag.org/content/3/17/eaat1893#BIBL
PERMISSIONS	http://www.sciencemag.org/help/reprints-and-permissions

Use of this article is subject to the Terms of Service